INFRARED DETECTOR ARRAYS, UNCOOLED

Infrared imaging has demonstrated itself to be a vital aspect of modern warfare. Infrared (IR) imaging has been used for surveillance, targeting, and night vision. The civilian applications of infrared imaging for security, thermography, and night vision in transportation are becoming increasingly widespread. The key factor limiting the adoption of widespread civilian applications of infrared imaging is the high cost associated with cryogenically cooled IR detector arrays. More recently, thermal imaging arrays capable of operating at or near room temperature without costly cryogenic refrigeration have been developed. These systems are less expensive than their cryogenic counterparts; however, they are not yet inexpensive enough to be feasible for mass consumer applications. However, as uncooled infrared imaging technol-

J. Webster (ed.), *Wiley Encyclopedia of Electrical and Electronics Engineering*. Copyright © 1999 John Wiley & Sons, Inc.

ogy develops, low-cost systems will be developed, enabling night vision in automobiles, significantly improving automobile safety by allowing the driver to see beyond the range of the headlights and enabling other mass consumer applications in transportation, security, and medicine to be realized.

Infrared detectors can be generally classified as belonging to one of two types. There are photon detectors and thermal detectors. Photon detectors generally operate using the photovoltaic effect or photoconductivity. In either case, a photon detector relies upon the absorption of a quantum of light by an electron. The electron then may be excited to a state where it can be transported over a barrier; or, more commonly, it results in the generation of electron–hole pairs, allowing for increased conductivity (photoconductivity) or a shift in the quasi-Fermi levels (photovoltaic). Photon detectors do not possess a high detectivity at room temperature due to the noise associated with the dark current. To minimize the dark current, photon detectors are generally cooled to cryogenic temperatures by submersion in liquid helium or liquid nitrogen or by employing a closed-cycle refrigerator. The necessity of cryogenic cooling significantly increases the system cost and the complexity of an infrared camera. Most infrared photon detectors are based upon HgCdTe devices or silicon Schottky barrier diodes.

In contrast, thermal detectors operate by utilizing the heat generated by the absorption of the photon flux to change temperature. The change in the temperature is associated with a change in a measurable electrical property of the material such as the electrical resistance (bolometer), spontaneous polarization (pyroelectric detector), or Fermi level (thermocouple). To maximize the response of a thermal detector, it is important to maximize the temperature change with respect to the energy absorbed by the photon flux. To this end, it is important that a minimal amount of heat be lost through conduction away from the detector. The detector is, therefore, usually thermally isolated from its surrounding as much as possible to achieve a large responsivity. This can be achieved in microdetectors by micromachining the detectors to be suspended above the substrate and placing the detector in vacuum, thereby minimizing the amount of heat lost to the substrate by conduction. Typically, a thermal conductance of 10^{-7} W/K is achieved. In addition, microfabrication allows detectors with a very low thermal mass (specific heat) (10^{-10} J/K) to be fabricated, again providing large temperature changes in the detecting element with respect to the incident photon energy. Thermal detectors do not suffer from noise associated with dark current; therefore, high-detectivity detectors ($D^* \approx 10^{10}$ cm-Hz$^{1/2}$/W) operating at room temperature are possible.

BOLOMETRIC DETECTORS

Theory of Bolometer Operation

A bolometer operates through the temperature-dependence of the resistance of the sensitive element or thermometer. As the temperature of the bolometer changes with the energy carried by the incident photon flux, the resistance changes, thereby giving a measurable signal when current biased. The relative magnitude of the change in the electrical resistance is known as the temperature coefficient of resistance (TCR). The TCR is given by

$$\mathrm{TCR} = \beta = \frac{1}{R}\frac{dR}{dT} \tag{1}$$

Performance improves with the magnitude of the TCR. Metals (1,2) were originally used as bolometers; however, their TCR is limited to 0.5% K^{-1}, thereby limiting their responsivity and detectivity. At present, practical microbolometers are based upon semiconductors such as germanium (3), amorphous silicon (4), and vanadium oxide (5–9). In addition, more recently, semiconducting YBaCuO has been proposed (10–13).

The responsivity of a bolometer—that is, the output signal voltage per unit incident infrared power—is given by (14)

$$R_V = \frac{I_b R \beta \eta}{G(1+\omega^2\tau^2)^{1/2}} \tag{2}$$

where I_b is the bias current, R is the direct current (dc) resistance, η is the absorptivity, G is the thermal conductance between sensitive element and the substrate, ω is the angular modulation frequency of the incident radiation, and τ is the thermal response time which is given by C/G. C is the heat capacity (thermal mass) of the sensitive element. Therefore, for high responsivity, high dR/dT, low G, and low ω ($\omega\tau \ll 1$) are required. Silicon micromachining techniques can be employed to create an air-gap bridge under the detector to provide low thermal conductance and heat capacity (15–17).

The detectivity D^* is determined by the ratio of the responsivity R_V to the noise voltage V_n:

$$D^* = \frac{R_V\sqrt{\Delta f A}}{V_n} \tag{3}$$

where Δf is the amplifier frequency bandwidth, V_n is the total noise voltage of the detector, and A is the area of the detector (thermometer).

The noise voltage, V_n, is determined by the sum of the contributions due to the background noise produced by the blackbody emissions of the surroundings, the temperature fluctuation noise due to thermodynamic fluctuations in the isolated thermal mass, and the noise generated by the thermometer or sensitive element. The noise generated by the thermometer includes Johnson noise and the low-frequency noise of the material. The respective noise contributions may be calculated from the following relations.

The temperature fluctuation noise is due to temperature fluctuations resulting from the exchange thermal conduction of isolated thermal detector with the substrate. The temperature fluctuation noise voltage, ΔV_{TF}, is calculated from

$$\frac{\Delta V_{\mathrm{TF}}}{\sqrt{\Delta f}} = \frac{2k_B^{1/2} I_b R \beta T_D}{G^{1/2}(1+4\pi^2 f^2 \tau^2)^{1/2}} \tag{4}$$

where T_D is the detector temperature and k_B is Boltzmann's constant. The background voltage noise, ΔV_{BG}, results from the radiative exchange of the detector with the surroundings. For a detector surrounded by a uniform blackbody at temperature T_B, the background voltage noise may be calculated from

$$\frac{\Delta V_{\mathrm{BG}}}{\sqrt{\Delta f}} = \frac{I_b R\beta[8A\eta\sigma k_B(T_D^5+T_B^5)]^{1/2}}{G(1+4\pi^2 f^2\tau^2)^{1/2}} \tag{5}$$

where A is the total surface area of the detector and σ is the Stefan–Boltzmann constant.

The voltage noise generated by the sensitive material or thermometer occurs due to the Johnson noise associated with the resistance of the detector plus the $1/f$ noise of the material. The Johnson noise voltage is given by

$$\frac{\Delta V_J}{\sqrt{\Delta f}} = \sqrt{4k_B T_D R} \tag{6}$$

The $1/f$ noise may originate due to a variety of physical processes. The magnitude of the $1/f$ noise must be determined empirically for a given material used as the thermometer. The $1/f$ noise is often determined by material processing parameters because it often relates to the number of traps throughout the volume or at the surface of the thermometer layer. In general, the Hooge formula (18) provides a relation for the voltage spectral density associated with the $1/f$ noise. The noise voltage is taken as the square root of the voltage spectral density. The Hooge formula is given by

$$S_V = \frac{\alpha V^2}{fN} = \frac{\Delta V_{1/f}^2}{\Delta f} \tag{7}$$

Here, α is Hooge parameter which provides the relative magnitude of the $1/f$ noise, V is the dc voltage, and N is the total number of independent fluctuators. The fluctuators are the scattering centers creating the noise. In bulk materials, the fluctuators are often distributed evenly throughout the volume of the material; however, in the case of thin films, as employed in microbolometers, the dominant scattering mechanism is often associated with surface states (19) and the fluctuators are distributed over the surface of the thin film.

The corner frequency occurs where the $1/f$ noise merges with the Johnson noise floor. The power-normalized corner frequency reflects the inherent noise in the bolometer and is a useful comparison for the noise in different types of bolometers. By equating the Hooge formula to the Johnson noise, the power-normalized corner frequency is given by

$$\frac{f_c}{I_b^2 R} = \frac{\alpha}{4k_B T_D N} = \frac{1}{4k_B T_D}\left(\frac{\Delta V_{1/f}}{V}\right)^2 \frac{f}{\Delta f} \tag{8}$$

The total noise voltage V_n is provided by the sum of squares of the contributions due to temperature fluctuation noise, background noise, Johnson noise, and $1/f$ noise:

$$\frac{V_n^2}{\Delta f} = \frac{\Delta V_{1/f}^2}{\Delta f} + \frac{\Delta V_{\mathrm{TF}}^2}{\Delta f} + \frac{\Delta V_{\mathrm{BG}}^2}{\Delta f} + \frac{\Delta V_J^2}{\Delta f} \tag{9}$$

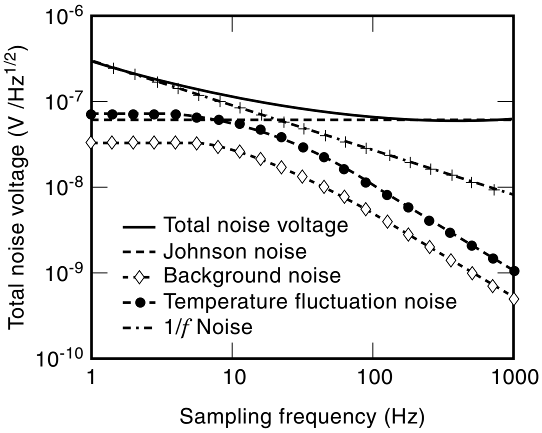

Figure 1. A plot of the noise components and total noise for a microbolometer as a function of sampling frequency. The following parameters were used in constructing the plot: $\beta = 3.5\%\ \mathrm{K}^{-1}$, $R = 235\ \mathrm{k}\Omega$, $\eta = 1$, $C = 0.7$ nJ/K, $G = 70$ nW/K, $\tau = 0.01$ s, $T_{\mathrm{D}} = 300$ K, $A = 50\ \mu\mathrm{m} \times 50\ \mu\mathrm{m}$, $\alpha/N = 10^{-12}$, and $I_b = 1\ \mu\mathrm{A}$.

The relative magnitude of the different noise components is plotted in Fig. 1. As can be seen by the plot, the $1/f$-noise component dominates the noise voltage at low frequencies, while at high frequencies the Johnson noise dominates. A material with lower $1/f$ noise would see the contributions due to temperature fluctuation noise and background noise play a greater role at intermediate frequencies. It is important to note that the magnitude of the $1/f$ noise, temperature fluctuation noise, background noise, and responsivity are proportionate to the bias current I_b. At zero bias, the noise voltage is determined by the Johnson noise. However, there is no responsivity. As I_b is increased, the responsivity is increased as well as the contributions due to background, temperature fluctuation, and $1/f$ noise. While the magnitude of these noise components remain much less than the Johnson noise, the detectivity increases at the sampling frequency of interest, until the magnitude of these noise components starts to dominate over the Johnson noise. At this point, both the responsivity and the device noise are increasing with the current bias, thereby leading to a saturated, maximum detectivity. In imaging arrays, image quality dictates operating the bolometers in the Johnson noise regime where the contributions from the temperature fluctuation, background, and $1/f$ noise are small, resulting in an operating detectivity less than the maximum. The background and temperature fluctuation noise components have the same cutoff frequency due to the thermal time constant as the responsivity, while the Johnson noise continues to high frequencies. To decrease the total Johnson noise voltage contribution, a low-pass filter is used.

The corresponding responsivity and detectivity are plotted versus sampling frequency in Fig. 2. The plot shows that the responsivity is constant at low sampling frequencies and decreases at higher frequencies due to the thermal time constant of the thermal isolation structure. The detectivity is reduced slightly at low frequencies due to the presence of the $1/f$ noise, and it reaches a maximum as the $1/f$ noise merges with the Johnson noise before decreasing with the thermal time constant of the bridge structure. Detectivities in the range of 10^9 cm-Hz$^{1/2}$/W to 10^{10} cm-Hz$^{1/2}$/W are achievable with state-of-the-art uncooled microbolometers.

The signal-to-noise ratio of the bolometer is often expressed in terms of a noise equivalent power (NEP), which is the incident photon power required to produce a voltage signal equal to the total noise voltage. The NEP can be calculated from the ratio of the total voltage noise divided by the responsivity. The NEP of uncooled microbolometers is typically higher than cooled IR detectors simply because of the operation at elevated temperatures:

$$\mathrm{NEP} = \frac{V_n}{R_V} \tag{10}$$

When the microbolometers are integrated into arrays, the ability to have high detectivity is important, but the most important figure of merit is the ability to resolve small temperature differences in the field of view. This figure of merit is expressed as the noise equivalent temperature difference (NETD). The NETD is given by

$$\mathrm{NETD} = \frac{4}{\pi}\left[\frac{(F/\#)^2\sqrt{\Delta f}}{D*(\partial L/\partial T)_{\lambda_1-\lambda_2}\sqrt{A_d}}\right] \tag{11}$$

where, $F/\#$ is the F number of the optics, $\partial L/\partial T$ is the rate of change of the radiance of the object with temperature, and A_d is the area of the detector. Most thermal imaging systems operate either in the 3 μm to 5 μm atmospheric window or the 8 μm to 14 μm atmospheric window, where $(\partial L/\partial T)_{\lambda_1-\lambda_2}$ can be shown to be equal to 2×10^{-5} W/cm^2-K and 2.6×10^{-4} W/cm^2-K, respectively.

Evaluating Eq. (11) in the case of temperature fluctuation noise limited detectivity, the NETD is given by

$$\mathrm{NETD}_{\mathrm{TF}} = \frac{8}{\pi}\left[\frac{T_{\mathrm{D}}(F/\#)^2\sqrt{Gk_{\mathrm{B}}\Delta f}}{\eta(\partial L/\partial T)_{\lambda_1-\lambda_2}A_d}\right]$$

The $\mathrm{NETD}_{\mathrm{TF}}$ therefore decreases as the square root of the thermal conductance away from the bolometer and is directly proportional to the detector temperature. As the thermal conductance of the bolometer is decreased, the temperature fluctuation noise decreases below the background noise. In this case, the NETD would be limited by the background noise associated with the radiative energy exchange between the bolometer and its surroundings. The NETD in this case is given by

$$\mathrm{NETD}_{\mathrm{BG}} = \frac{8}{\pi}\frac{(F/\#)^2}{(\partial L/\partial T)_{\lambda_1-\lambda_2}}\sqrt{\frac{2\sigma k_{\mathrm{B}}(T_{\mathrm{D}}^5+T_{\mathrm{B}}^5)\Delta f}{\eta A_d}}$$

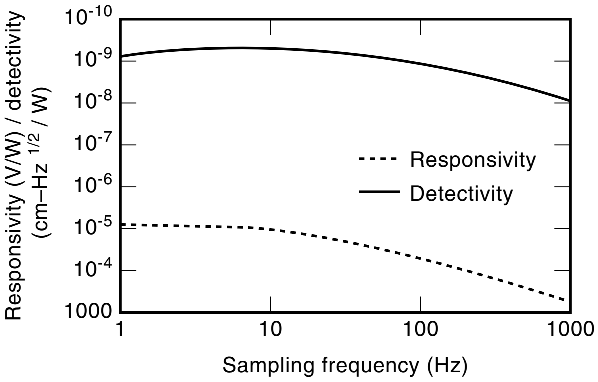

Figure 2. A plot of typical microbolometer responsivity and detectivity of sampling frequency using the same parameters described in Fig. 1.

The $\mathrm{NETD}_{\mathrm{BG}}$ is independent of the thermal isolation but depends upon the temperature of the detector and background. At room temperature, the $\mathrm{NETD}_{\mathrm{BG}}$ is calculated to be 5 mK in the 3 μm to 5 μm band and 0.4 mK in the 8 μm to 14 μm band. In performing these calculations, it is assumed that the system would have $F/1$ optics, $\eta = 1$ absorptivity, 40 μm × 40 μm pixel size, bandwidth $\Delta f = 30$ Hz, device temperature $T_{\mathrm{d}} = 300$ K, and background temperature $T_{\mathrm{B}} = 300$ K. NETDs less than 30 mK have been measured with uncooled microbolometer imaging arrays. This result is approaching the background limited noise performance. It is an impressive performance considering the approximations made in the calculations presented here. Reference 30 provides a more detailed discussion on the calculation of NETD and the dependence upon thermal isolation and detector temperature.

Vanadium Oxide Microbolometer Arrays

Vanadium oxide (VO_x) microbolometer technology was developed by Honeywell (9) and is currently being used under license by Raytheon-Amber (8), Hughes Aerospace (5), Rockwell International (7), and Lockheed-Martin (6). The technology employed by these companies varies mainly in terms of the readout circuitry employed to operate the microbolometer arrays, the method of fabricating the thermal isolation structures, and the geometry of the detector arrays fabricated. A description of the VO_x focal plane array (FPA) technology at Hughes Santa Barbara Research Center (SBRC) follows.

SBRC has been developing uncooled microbolometer FPAs since Hughes Aircraft Company licensed the microbolometer detector technology from Honeywell (5) in 1993. SBRC has focused on developing high-performance readout integrated circuits (ROICs) and improving the microbolometer detector structure and fabrication process. These improvements have included increases in pixel thermal isolation, optical fill-factor, and temperature coefficient of resistance. Simultaneously, the fabrication process has been simplified to achieve better yields and faster cycle times.

A scanning electron micrograph of the microbolometer pixels fabricated with the dry sacrificial etch process and the optimized $\mathrm{Si_3N_4}$ is shown in Fig. 3. A self-aligned leg etch process is being used to reduce the microbolometer support leg width to less than 2 μm. This has increased the thermal isolation by a factor of two while allowing area for increased detector fill-factor. A polyamide sacrificial layer has been implemented in place of the baseline $\mathrm{SiO_2}$ sacrificial layer. The polyamide material allows the use of a dry sacrificial etch rather than the wet HF-based etch used in the baseline process. The elimination of the wet etch has dramatically simplified the microbolometer fabrication process. The dry etch process has an essentially zero etch rate of (a) the $\mathrm{Si_3N_4}$ used for the bridge and (b) the oxides and metal layers used in the readout substrates.

The dry sacrificial etch process also facilitated performance improvements in the microbolometer responsivity. The thick-

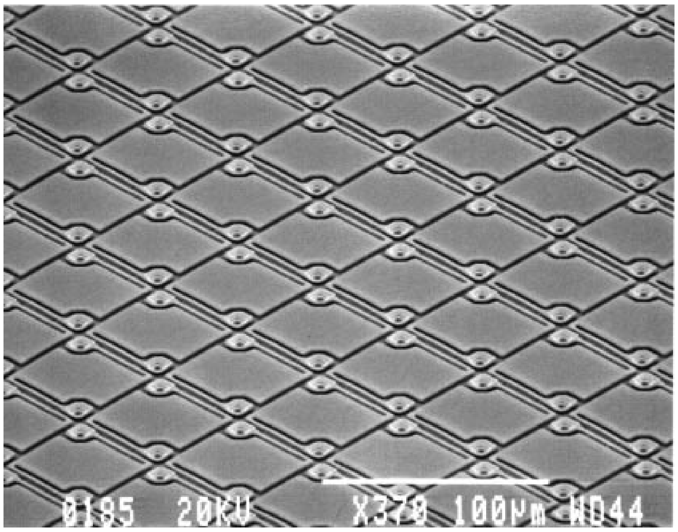

Figure 3. Scanning electron micrograph of microbolometer pixels fabricated at SBRC using polyamide sacrificial etch process. From Hughes Santa Barbara Research Center with permission. © 1997, Santa Barbara Research Center.

ness of the Si_3N_4 layers has been reduced without sacrificing device yield. Si_3N_4 bridge thicknesses as thin as 360 nm have been successfully demonstrated using the dry etch process. The deposition process of the Si_3N_4 process has been optimized for throughput and thermal properties. The nitride deposition process can complete a 20-wafer lot in about 1 h. The deposition process has also been optimized to produce films with low stress and low thermal conductivity. The thermal conductivity of the Si_3N_4 is only about 0.8 $W\text{-}m^{-1}\text{-}K^{-1}$. This represents over a factor-of-two reduction of thermal conductivity compared with the baseline material.

An advanced microbolometer fabrication process has been employed to build high-image quality IR FPAs. These FPAs have a 320 × 240 format with 50 μm × 50 μm pixels and are based on a complementary metal oxide semiconductor (CMOS) read-out integrated circuit (ROIC). The ROIC uses on-chip clock and bias generation to provide a simple electrical interface requiring only three clocks and five bias levels. The FPA has a single video output and can operate at frame rates up to 60 Hz. The SBRC-151 ROIC operates in an electronically scanned format and pulse-biases each pixel. It performs two levels of on-chip offset correction to minimize spatial nonuniformity of the FPA pixels. The on-chip correction allows the use of a high detector bias (4 V) and on-chip gain without saturation of the output range. The readout utilizes a differential architecture throughout the signal chain in order to minimize sensitivity to bias fluctuation and external noise sources. These features give the SBRC-151 very high responsivity and good extraneous noise immunity. The ROIC also incorporates an on-chip temperature compensation capability in order to minimize temperature stabilization requirements. The various operational and test modes of the chip are controlled through a 32-bit serial programmable interface. The ROIC was specifically designed to accommodate a wide range of detector impedances without any degradation of sensitivity. The ROIC will operate with pixel impedances ranging from 10 kΩ to 200 kΩ with little degradation in performance.

The microbolometer FPAs are mounted in vacuum packages with a single-stage thermoelectric cooler for temperature stabilization. An antireflective-coated germanium (Ge) window is used to achieve high transmission in the 8 μm to 14 μm spectral region.

The SBRC-151 FPAs have been integrated into several camera systems including the long-wavelength staring sensor (LWSS) developed by Hughes Sensors and Communications Systems (SCS). The LWSS is a prototype military IR camera for portable applications. The camera was designed to achieve low-power consumption in order to maximize battery life. The camera utilizes a 50 mm focal length $f/0.7$ Ge lens assembly with a broadband AR coating. The LWSS camera provides memory for the coarse on-chip correction terms as well as the gain and offset nonuniformity correction terms.

The LWSS sensor has been used for imaging demonstrations and radiometric testing of the SBRC-151 FPAs. The Hughes LWSS camera was independently evaluated at the US Army Night Vision and Electronic Sensors Directorate (NVESD). The NVESD performed measurements of NETD, minimum resolvable temperature (MRT), and three-dimensional noise. An NETD of 24 mK was measured with the $f/0.7$ optics while an NETD of 42 mK was measured with the optics stopped down to $f/1.0$. Figure 4 presents MRT measurements obtained by NVESD using the $f/0.7$ optics. The vertical MRT ranged from 48 mK at the Nyquist frequency (f_N) to 16 mK at low spatial frequency (0.30 f_N). The horizontal MRT ranged from 59 mK at the f_N to 17 mK at 0.30 f_N. The NVESD measured spatial camera noise was less than 50% of the temporal noise. Further optimization of the FPA and camera is expected to produce NETD values of <20 mK for $f/1.0$ apertures. The scene dynamic range of the camera is greater than 50 K with the $f/0.7$ optics and greater than 100 K with the $f/1.0$ optics.

The pixel operability for the same FPA was measured to be 99.2%. An operable pixel is defined as one with an $f/0.7$ NETD less than 50 mK. The instantaneous scene temperature dynamic range of the pixels is typically about 50 K with $f/0.7$ optics and about 100 K with $f/1.0$ optics. A single-frame

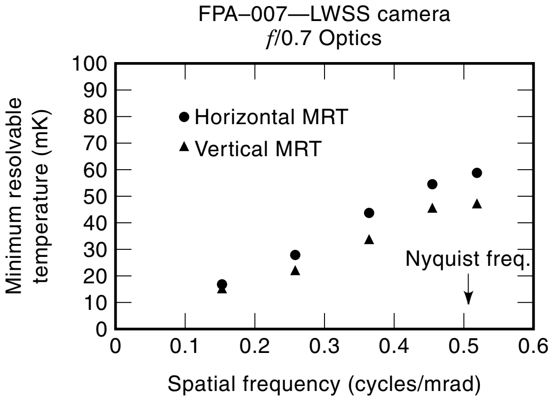

Figure 4. Minimum resolvable temperature data taken at US Army NVESD on Hughes LWSS manportable uncooled sensor. NVESD measured an NETD value of 24 mK on the sensor. (From Hughes Santa Barbara Research Center, with permission. © 1997, Santa Barbara Research Center.)

Figure 5. Single frame of night imagery of Mission Santa Barbara obtained with Hughes LWSS portable uncooled sensor. (From Hughes Santa Barbara Research Center, with permission, © 1997, Santa Barbara Research Center.)

example of night imagery obtained from the LWSS camera is shown in Fig. 5.

Prospects for Semiconducting Yttrium Barium Copper Oxide (YBaCuO) Microbolometer Arrays

Although VO_x technology has obtained impressive performance, there are difficulties associated with the deposition of the material across the wafer with uniform resistivity and TCR across the wafer. This, combined with the relatively low TCR which necessitates a large current bias and thereby power dissipation, has made the search for an alternative material. In general, the bolometric material should be easily deposited and patterned using standard semiconductor processing equipment. The processing of the bolometer material must also be compatible with Si micromachining processes and be compatible with the CMOS readout circuitry, which is typically fabricated underneath the bolometer array. These criteria require that the material be deposited uniformly over the wafer with only small spatial variations in the resistivity and TCR. Furthermore, all the processing would ideally be conducted at temperatures less than 300°C so the underlying CMOS readout circuitry is not degraded. In addition, the bolometer material should have a high TCR to allow for small bias currents and, hence, low power dissipation and long battery life for the IR camera. YBaCuO is one material that satisfies these criteria.

YBaCuO is best known as a high-temperature superconductor. The optical and electronic properties of $YBa_2Cu_3O_{6+x}$ are determined by its oxygen stoichiometry. For $x \approx 1$, YBaCuO possesses an orthorhombic crystal structure, exhibits metallic conductivity, and becomes superconductive upon cooling below its critical temperature. As x is decreased to 0.5, the crystal structure undergoes a phase transition to a tetragonal structure and it exhibits semiconducting conductivity characteristics because it exists in a Fermi glass state. As x is decreased further below 0.3, YBaCuO becomes a Hubbard insulator with a well-defined energy gap on the order of 1.5 eV (20). The unit cell consists of three CuO planes in the a–b plane sandwiched between two planes containing BaO and one plane containing Y atoms along the c-direction. Each layer consists of corner-sharing CuO_n polyhedra held together by the Y plane. As x is increased, O is randomly introduced to the O(1) sites creating carriers and simultaneously results in disorder, leading to formation of localized states in the CuO planes.

Several reports exist in the literature on transport, Hall effect, and dielectric measurements of the semiconducting YBaCuO thin films (21–24). A brief summary of results is presented in Table 1.

In the semiconducting state, YBaCuO exhibits a relatively large TCR (~3 to 4% K^{-1}) over a 60 K temperature range near room temperature. The large TCR, combined with the ease of thin film fabrication that is compatible with CMOS processing, makes YBaCuO attractive to microbolometer applications.

The YBaCuO thin films, whose data are reported here, were deposited by radio frequency (RF)–magnetron sputtering in a CVC-601 sputtering system at ambient temperature using commercially available $YBa_2Cu_3O_{6+x}$ sputter targets (10–13). Microbolometer array test structures were fabricated by depositing the YBaCuO IR-sensitive element onto a suspended bridge. A scanning electron micrograph of a typical array is shown in Fig. 6. In this case, the bridge structures were fabricated removing the Si underneath a 1500 nm thick SiO_2 by etching with a $HF:HNO_3$ solution through trench cuts in the oxide layer. A 40 nm thick MgO buffer layer was deposited by RF-magnetron sputtering, followed by the 200 nm thick YBaCuO film. The MgO buffer layer was used to act as a barrier against any interaction between YBaCuO and the substrate because some evidence of Cu diffusing into silicon had been observed earlier. In addition, lower noise characteristics have been observed in YBaCuO films deposited on MgO. The effect of encapsulating YBaCuO in MgO or other passivating films has yet to be tried. The YBaCuO and MgO was then patterned to define IR-sensitive areas by the wet etching. A 300 nm thick Au film was sputter-deposited and etched to form the contact pads and leads.

The two-probe resistance values for array pixels were found to vary roughly from 2 MΩ to 10 MΩ depending on geometry for these devices. The TCR (or β) was calculated from the resistance versus temperature characteristics. For pixel #2 of the same array, β was found to vary from ~2.99% to 3.37% in the 282 K to 312 K range with a room tempera-

Table 1. Selected Properties of Semiconducting YBaCuO[a]

Parameter	Value
Conductivity activation energy (near room temperature)	$E_a \approx 0.2$–0.3 eV
Relative dielectric constant ($T = 298$ K)	$\varepsilon_r = 87$–500
Typical resistivity ($T = 298$ K)	$\rho = 1$–100 Ω-cm
Hall carrier concentration n_H ($T = 298$ K)	10^{16}–10^{20} cm^{-3} p-type
dR/dT ($T = 298$ K)	8×10^3 Ω/K
Temperature coefficient of resistance ($T = 298$ K)	-3.9% K^{-1}
Voltage noise at 1 μA current bias and 30 Hz (1/f noise regime)	$V_n/\Delta f < 0.75$ μV/$Hz^{1/2}$

[a] The wide range in some of the parameters is due to the varying oxygen content.

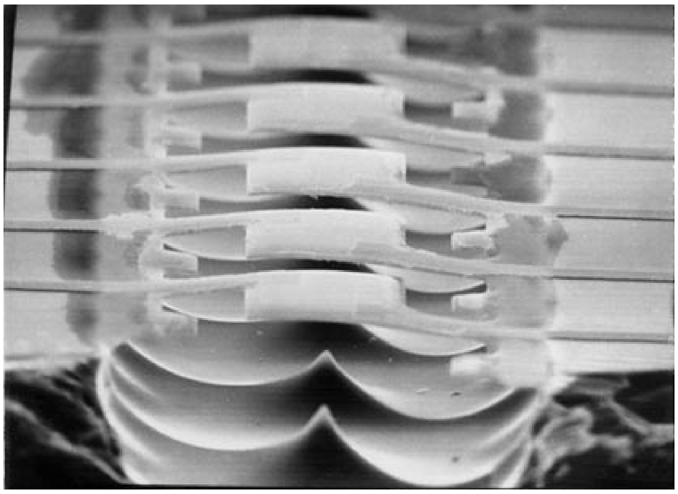

Figure 6. Scanning electron micrograph of a one-dimensional YBaCuO microbolometer array fabricated on an oxidized Si substrate. The YBaCuO IR-sensitive element is suspended on the micromachined SiO_2 bridge and is contacted by gold leads running along the arms of the bridge. The pixel size is approximately 40 μm × 40 μm.

ture value of 3.25%. The wafer average value of β was 3.5% and varied less than 10% across the wafer.

The optical response of the YBaCuO microbolometer arrays was measured by using a 1450 K blackbody source. The net usable range of this broad-band system was ~0.8 μm to 12 μm. Narrow-band spectral analysis was performed with an Oriel MS-257 monochromator/spectrograph. The samples were characterized under both front-side and backside (through the substrate) illumination with mechanically chopped infrared light. Room temperature measurements of the responsivity, R_V, and detectivity, D^*, were performed in air. The temperature-dependent measurements were performed in a cryostat evacuated to a pressure of 30 mTorr. The response of the YBaCuO devices was calibrated against a pyroelectric detector with $R_V = 1000$ V/W. In Fig. 7(a), typical room-temperature responsivity R_V is displayed at different bias levels of 0.126 μA to 0.79 μA. The responsivity was linear with respect to the bias current implying a true bolometric behavior. At high frequencies, R_V decreased in accordance with Eq. (2). A thermal time constant, $\tau \sim 0.7$ ms, was obtained by fitting this relation to the measured response. A room-temperature value of $G/\eta = 2.6 \times 10^{-5}$ W/K was computed using Eq. (1) and the values of measured β and R, computed τ and the applied bias current I_b. The thermal conductance G of the suspended structure was measured by the resistive or Joule heating method to be 7.41×10^{-6} W/K. From the measurement of the thermal conductance and time constant the thermal mass C was calculated to be ~10^{-8} J/K. Using the value of G/η calculated from the responsivity data and G from Joule heating, a value of absorptivity η for the YBaCuO film was estimated to be about 29%. However, in order to obtain a more realistic figure, a direct measurement of absorptivity and reflectivity characteristics for this material needs to be performed.

Noise characteristics were also investigated to evaluate the performance of the bolometer in terms of detectivity D^*. D^* is displayed in Fig. 7(b). At zero-bias or very low currents ($I_b <$ 0.1 μA), the noise spectrum showed essentially the Johnson (or $4kTR$) level. A $1/f$ noise was observed at low frequencies (~2 μV/Hz$^{1/2}$ at 30 Hz for 0.79 μA), which caused D^* to decline slightly. At higher frequencies (above ~300 Hz for 0.79 μA), the excess noise spectral density merged with the Johnson noise floor of ~0.4 μV/Hz$^{1/2}$. From the point of view of detectivity, the optimum range for chopping frequency was found to be about 70 Hz to 200 Hz, above which the cutoff due to τ caused R_V and, hence, D^* to fall below their maxima. A plausible cause of $1/f$ noise was the contact resistance between gold metallization and the YBaCuO film. If this is true, then decreasing the contact resistance would bring the low-frequency noise down to the Johnson noise level, improving the performance of these devices by an order of magnitude.

It is important to note that the measured thermal conductance of the YBaCuO microbolometer test structures is approximately two orders of magnitude larger than the state-of-the-art obtained elsewhere for amorphous-Si and VO_x bolometers. This would imply that detectivities in the range of 10^9 to 5×10^9 cm-Hz$^{1/2}$/W are achievable if state-of-the-art thermal isolation structures were employed. This is comparable to VO_x and amorphous-Si devices. It is also important to note that the top surface of the YBaCuO bolometers was not passivated and likely suffers from a larger $1/f$ noise component than if the YBaCuO film was totally encapsulated. VO_x technology uses Si_3N_4 encapsulation, in part to reduce the $1/f$ noise present in the film. For YBaCuO, it has been observed that utilizing the MgO buffer layer reduces the $1/f$ noise present in the film, and it is likely that MgO encapsulation would further reduce the $1/f$ noise and lead to higher detectivities.

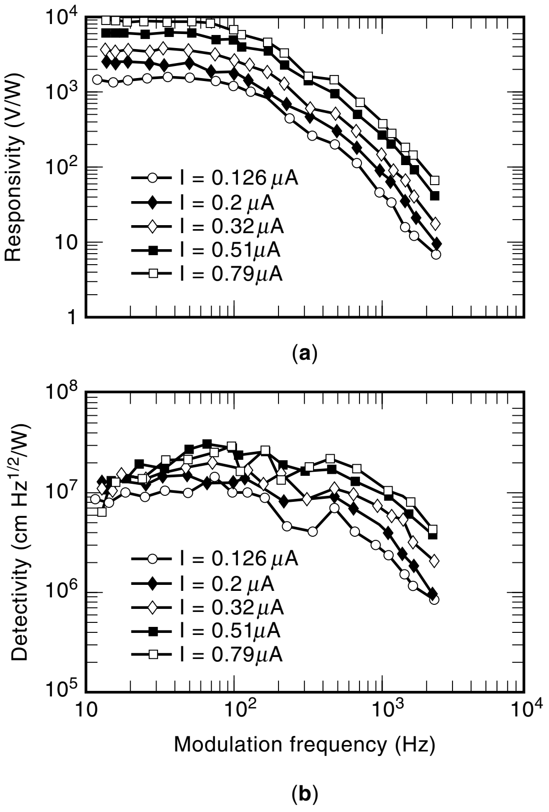

Figure 7. (a) Responsivity and (b) detectivity of 40 μm × 40 μm YBaCuO microbolometer pixel as a function of IR chopping frequency at different current biases.

Table 2. A Comparison Between Uncooled Bolometer Technologies

Material	TCR ($\% \text{ K}^{-1}$)	$f_c/4k_BT$ (Hz/W)
VO_x	1.5–4	1.2×10^{-13}
Amorphous Si	1.8	4×10^{-12}
Semiconducting YBaCuO	3–4	4×10^{-13}

[a] From Refs. 6, 10–13, and 25.

The different microbolometer technologies are compared in Table 2 with respect to the TCR and corner frequency.

PYROELECTRIC IR DETECTORS

Theory of Pyroelectric Detector Operation

A pyroelectric detector operates through the temperature-dependence of the spontaneous polarization of the material. As the polarization changes with temperature, the surface charge on a pyroelectric capacitor changes, resulting in a measurable pyroelectric current,

$$I = pA\,dT/dt \tag{12}$$

where p is the pyroelectric coefficient, A is the capacitor area, T is temperature, and t is time. The pyroelectric capacitor is connected to a preamplifier. A typical pyroelectric detector element of area A and dielectric thickness d connected to a read-out amplifier is shown in Fig. 8. Radiation with power $\Phi(t)$ modulated at frequency ω is incident on surface of the element. The absorptivity of the detector is η. The detector element has a thermal capacity C and a thermal conductance to the substrate G. Thus, the temperature change, ΔT, resulting from the incident radiant flux can be expressed as

$$C\frac{d\Delta T}{dt} + G\Delta T = \eta\Delta\mathbf{\Phi}(t) \tag{13}$$

where the temperature of the detector element is $T(t) = T_{\text{eq}} + \Delta T(t)$, modulated by the radiation flux

$$\mathbf{\Phi}(t) = \mathbf{\Phi}_{\text{eq}} + \Delta\mathbf{\Phi}(t) = \mathbf{\Phi}_{\text{eq}} + \mathbf{\Phi}_0 e^{j\omega t} \tag{14}$$

The solution to Eq. (13) is

$$\Delta T = T_0 e^{j\omega t} \tag{15}$$

with

$$T_0 = \frac{\eta}{G}\frac{1}{\sqrt{1+\omega^2\tau_{\text{th}}^2}}\mathbf{\Phi}_0 \tag{16}$$

The thermal time constant τ_{th} is defined as $\tau_{\text{th}} = C/G$.

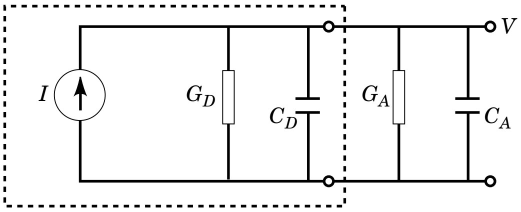

Figure 8. The equivalent circuit depicting the detector and the read-out amplifier.

The response is usually read out by an amplifier that can be shown as a combination of conductance G_A and capacitance C_A in parallel with the detector conductance G_D and capacitance C_D (Fig. 8). If the induced pyroelectric current I is read out as voltage V, then

$$C_E\frac{dV}{dT} + G_E V = I = pA\frac{dT}{dt} \tag{17}$$

Here, $C_E = C_D + C_A$, and $G_E = G_D + G_A$ are the equivalent electrical capacitance and conductance of the circuit in Fig. 1. Solving Eq. (17) with Eq. (15), we find

$$\Delta V(t) = V_0 e^{j\omega t} \tag{18}$$

and

$$V_0 = \frac{pA}{C_E}\frac{\omega\tau_e}{\sqrt{1+\omega^2\tau_e^2}}T_0 \tag{19}$$

The electrical time constant, τ_e, is expressed by $\tau_e = C_E/G_E$. Combining Eqs. (16) and (19), voltage responsivity R_V can be obtained as (26–29)

$$R_V = \frac{V_0}{\mathbf{\Phi}_0} = \eta\frac{pA}{GG_E}\frac{\omega}{\sqrt{1+\omega^2\tau_{\text{th}}^2}\sqrt{1+\omega^2\tau_e^2}} \tag{20}$$

It should be noted that in solving Eqs. (13) and (17), phase terms were ignored.

To achieve a high responsivity, the detector is usually fabricated in a micromachined thermal isolation structure, minimizing G. As discussed before, the detectivity, $D^* = R_V\,(A\,\Delta f)^{1/2}/V_n$, gives the area-normalized signal-to-noise ratio in the frequency bandwidth Δf for the detector with V_n, the total noise voltage. Pyroelectric detectors experience Johnson noise, background noise in the photon flux, and temperature fluctuation noise. In practical cases, temperature fluctuation noise includes the background noise contributions and should be ideally the dominant noise source (30). The respective noise contributions may be calculated from the following relations (31).

Temperature or Radiation Noise. Even if the pyroelectric detector is in thermal equilibrium with its surroundings, it will experience agitation of charges due to (a) fluctuations in the incoming radiation and (b) exchange of heat due to convection and conduction. The temperature noise can be expressed as (26)

$$\frac{\Delta V_{\text{TE}}}{\sqrt{\Delta f}} = \frac{R_V\sqrt{4kT^2G}}{\eta} \tag{21}$$

If the temperature fluctuations due to convection and conduction are eliminated so that the only interchange of energy with the surroundings is by radiation, the detector is said to be background-limited, representing the highest achievable detectivity D^*_{BLIP} at a particular temperature (26,28).

$$D^*_{\mathrm{BLIP}} = \left(\frac{\eta}{16\sigma k T^5}\right)^{1/2} \tag{22}$$

Here, σ is Stefan's constant. At room temperature, for $\eta = 1$, the background-limited detectivity is 1.8×10^{10} cm Hz$^{1/2}$/W.

Johnson Noise. Johnson noise includes the thermal noise of the parallel conductances of the amplifier resistance and the alternating current (ac) conductance of the detector and is given by (26)

$$\frac{\Delta V_J}{\sqrt{\Delta f}} = \frac{\sqrt{4kTG_E}}{G_E\sqrt{1+\omega^2\tau_E^2}} \tag{23}$$

Since $G_E = G_A + G_D = G_A + \omega C_D \tan\delta$, depending on the frequency-dependence of the detector conductance, the spectral density of the Johnson noise in pyroelectric detection systems can take several shapes including $1/f$ and Lorentzian forms. The term $\tan\delta$ refers to the loss tangent of the material.

Johnson noise frequently dominates in pyroelectric detectors. For high frequencies such that ac conductance of the detector is much higher than the amplifier conductance, $\omega \gg (C_D \tan\delta/G_A)^{-1}$, $\omega \gg \tau_e^{-1}$, and $C_D \gg C_A$, the Johnson noise can be written as

$$\frac{\Delta V_J}{\sqrt{\Delta f}} = \left(4kT\frac{\tan\delta}{C_D}\right)^{1/2}\omega^{-1/2} \tag{24}$$

Consequently, for this specific case, the detectivity is given through Eqs. (3), (20), and (24):

$$D^* = \frac{\eta d}{\sqrt{4kT}}\frac{1}{\omega^{1/2}}\frac{p}{c'\sqrt{\epsilon\epsilon_0\tan\delta}} \tag{25}$$

Here, c' is the volume specific heat, d is the thickness of the pyroelectric element, ϵ is the relative permittivity of the pyroelectric material, and ϵ_0 is the permittivity of free space. Therefore, in order to maximize the detectivity for this region, it is desirable to maximize the last term in the above expression, which is sometimes referred to as F_D, one of the figures of merit for a pyroelectric detector (26,32).

The reader should be cautioned, however, that the conditions assumed in calculating Eq. (24) are frequently not applicable to small-area imaging detectors operating at camera frame frequencies (50 Hz or 60 Hz). As an example, consider a pyroelectric detector with $C_D = 5$ pF and with $\tan\delta = 0.01$, coupled to an amplifier with $C_A = 10$ pF and $G_A = 10^{-9}\ \Omega^{-1}$. In this case, the Johnson noise is determined by the amplifier circuit conductance and has a value of about 0.4 μV/Hz$^{1/2}$ at 30 Hz.

Amplifier Noise. An amplifier noise is produced in the electronic amplifier used in the read-out circuitry. It can be due to $1/f$ noise, generation recombination noise, or shot noise arising from the field-effect transistor (FET) gate leakage current. At camera frame frequencies, we expect this component to be less than the detector noise (26).

The total equivalent noise voltage is given as the squared sum of individual noise components, $V_n^2/\Delta f = \Delta V_{\mathrm{TF}}^2/\Delta f + \Delta V_J^2/\Delta f + \Delta V_A^2/\Delta f$. One of the most important issues in systems integration of pyroelectric detectors is to minimize the noise sources by careful matching of the amplifier to the detector, adjusting pyroelectric and dielectric properties of the pyroelectric material, and careful designing of the suspended structure and therefore thermal characteristics of the detector element.

A more relevant figure of merit for a complete IR camera, which takes into account the optics, focal plane array performance, and read-out electronics, is the noise equivalent temperature difference (NETD), as discussed earlier (30).

A list of commonly used materials for pyroelectric application include triglycene sulfate (TGS), lithium tantalate ($LiTaO_3$), $Ba_{1-x}Sr_xTiO_3$ (BST), $Pb_{1-x}La_x(Zr_{1-y}Ti_y)_{1-x/4}O_3$ (PLZT), and $PbTiO_3$. In addition, the semiconducting phase of yttrium barium copper oxide (YBaCuO) is a new promising pyroelectric material. Pyroelectric detectors can be operated without a bias below their Curie temperature (normal pyroelectrics) or at Curie temperature with bias (phase transition materials). The latter requires stringent bias and temperature stabilization requirements. Next generation uncooled pyroelectric detectors are required to operate without bias and temperature stabilization in a wide range of environmental conditions, and therefore should belong to the normal pyroelectrics family. In addition, it is desired to have a thin-film pyroelectric detector to be able to fully utilize the state-of-the-art micromachining technology for fabrication of focal plane arrays. Table 3 lists some of the commonly used pyroelectric materials and their pyroelectric coefficients.

The following sections will summarize some of the most commonly used pyroelectric detector technology for IR focal plane arrays.

Table 3. Room Temperature Pyroelectric Coefficients of Most Commonly Used Pyroelectric Materials

Material	p (μC/cm^{2}K)	Comments	Reference
TGS	0.028	Single crystal, bulk, normal pyroelectric	33
$LiTaO_3$	0.18	Single crystal, bulk, normal pyroelectric	34
KTN ($KTa_{1-x}Nb_xO_3$)	0.01	Polycrystalline, thin film, with bias	35
$PbTiO_3$ sol–gel	0.095	Polycrystalline, thin film, normal pyroelectric	36, 37
PScT ($Pb(Sc_{0.5}Ta_{0.5})O_3$)	0.5–0.6	Polycrystalline, thin film, phase transition material	38, 39
BST ($Ba_{1-x}Sr_xTiO_3$)	23	Ceramic, bulk, phase transition material	32, 40
PLT ($Pb_{1-3x/2}La_xTiO_3$)	0.065	Polycrystalline, thin film, normal pyroelectric	41
PLZT ($Pb_{1-x}La_x(Zr_{1-y}Ti_y)_{1-x/4}O_3$)	0.13–0.18	Ceramic, bulk, normal pyroelectric	42, 43
YBaCuO	18	Polycrystalline, thin film, normal pyroelectric	44, 45

Lead Titanate-Based Detectors

Research groups led by Polla (36) and Takayama (41) independently developed techniques for depositing $PbTiO_3$ thin films with high pyroelectric coefficient, detectivity, and fast response time. $PbTiO_3$ is a pyroelectric material with a Curie temperature of about 490°C. It is usually operated with no applied electric field and well below its transition temperature exploiting the normal pyroelectric effect where the rate of change in the spontaneous polarization with respect to temperature is measured. The latest-generation pyroelectric devices are thin films deposited on Si air-gap bridge structures for low thermal mass, low thermal conductivity, and hence increased responsivity. Since these devices are made on silicon, they can be directly integrated into silicon signal processing circuitry without the need of pump-bonds or wires. $PbTiO_3$ is typically deposited using sol–gel processing techniques with titanium–platinum (Ti–Pt) or Pt electrodes. Investigations carried out by Polla's group revealed a pyroelectric coefficient p of 95 $nC/cm^2 \cdot K$, a relative dielectric coefficient ϵ_r of 200, responsivity R_v of 10^4 V/W, and noise voltage V_n of 10^{-6} V/Hz$^{1/2}$ at 50 Hz for thin film $PbTiO_3$. These values compare favorably over the ones for other pyroelectric thin films like ZnO and $PbZrO_{0.54}Ti_{0.46}O_3$ (PZT). Test arrays of 64×64 $PbTiO_3$ elements, each 30×30 μm^2 in size, have been fabricated by surface micromachining techniques, on an NMOS readout circuitry, resulting in 1.2×10^4 V/W responsivity and 2×10^8 cm Hz$^{1/2}$/W normalized detectivity at 30 Hz (37). The measured response for a single pixel element was 90 $nC/cm^2 \cdot K$, while the response due to the combined effect was 60 $nC/cm^2 \cdot K$. Although this is far from background-limited operation, it shows promising progress toward lead titanate-based FPAs. There are, however, some problems. Reproducibility of $PbTiO_3$ thin-film deposition is low, requiring special attention to the deposition conditions and the chemical stability of electrode interfaces.

Barium Strontium Titanate Pyroelectric Detectors

Another state-of-the-art pyroelectric detector technology is $Ba_{1-x}Sr_xTiO_3$ thick films. Unlike $PbTiO_3$, $Ba_{1-x}Sr_xTiO_3$ is operated near the paraelectric–ferroelectric phase transition which can be adjusted to a temperature between 20°C and 30°C, depending on the value of x. The rate of change in the dielectric permittivity with respect to temperature is measured with an applied electric field. These detectors are also sometimes referred to as dielectric bolometers. Research groups at Raytheon–TI Systems fabricate IR cameras made of 245×328 pixel arrays with an array-average NETD of 0.070°C with $f/1.0$ optics (29,40). However, the present $Ba_{1-x}Sr_xTiO_3$ technology is a cumbersome bulk ceramic technology which requires grounding and polishing of ceramic wafers sliced from a boule, laser reticulation of pixels, multiple thinning, and planarization steps. The array is connected to the silicon readout circuit by compression bonds. The process suffers from (a) thermal isolation problems due to the thick mesa structure and (b) $Ba_{1-x}Sr_xTiO_3$ surface degradation due to the thinning procedure.

Prospects for Semiconducting Yttrium Barium Copper Oxide Pyroelectric Detectors

As discussed in the bolometer section, $YBa_2Cu_3O_{6+x}$ belongs to a class of copper oxides well known for their superconducting properties. Its conduction properties can be changed from metallic ($0.5 < x < 1$) to insulating ($0 \leq x \leq 0.5$) by suitably decreasing the oxygen content (20). Pyroelectric YBaCuO thin films have been fabricated by RF sputtering from a commercially available superconducting target on top of suspended SiO_2 bridges, using an $HF:HNO_3$ etch to remove the underlying Si (44). Detectivities as high as 10^8 cm-Hz$^{1/2}$/W have been measured for a thermal conductance $G = 10^{-5}$ W/K. Typically, $G \approx 10^{-7}$ W/K is achievable with the state-of-the-art surface micromachining techniques, indicating that detectivities of 10^{10} cm-Hz$^{1/2}$/W are possible using semiconducting YBaCuO. For a focal plane array made of 40×40 μm^2 pixels, operating in the 8 μm to 14 μm atmospheric window [$(\Delta P/\Delta T)_{\lambda_1-\lambda_2} = 2.6 \times 10^{-4}$ $W/cm^2 \cdot K$], employing $f/1$ optics with a transmittance close to 1, and chopped at 30 Hz chopper frequency, NETD values of 2 mK are achievable [Eq. (11)]. This performance is comparable to the background noise limited performance calculated for the microbolometer. YBaCuO combines an ease of fabrication that should lead to a reduction in cost. Pyroelectric coefficients as high as 18 $\mu C/cm^2$-K have been measured (45). The ability to pole the devices to obtain pyroelectric coefficients in this range was also demonstrated.

Strong pyroelectric effect in nonmetallic YBaCuO has also been confirmed by many researchers (46–48). Although the exact origin of the observed pyroelectric effect is not fully known at this time, it can be attributed to the noncentrosymmetric nature of the material with sufficiently long-range Coulomb ordering to give a net dipole moment (47). Pyroelectricity has been shown to exist in both metallic and insulating phases of $YB_2Cu_3O_{6+x}$ (44,49). Despite some controversy (49) with regard to the origin of pyroelectricity in YBaCuO, it is believed to be associated with symmetry-breaking in the unit cell due to the anharmonicity of the apex O(4) oxygen site which is present on the branch connecting the CuO_2 and basal planes of the $YB_2Cu_3O_{6+x}$ molecule (50). The cause of this behavior is probably due to the randomly filled O(5) *defect* site. The nonsymmetric displacement of O(4) mode results in a net polarization in the molecule with domains of dipoles scattered throughout the bulk of the material. This microscopic polarization appears at the macroscopic level when either strain by an externally applied electric field or mechanical strain acquired during the fabrication process provides the impetus for the domains to be lined up in one direction. In the *strain-poled* case, a sample would show pyroelectric behavior without the application of any poling bias.

Pyroelectricity is often associated with changes in individual crystal symmetry, leading to a net polarization. Mihailovic et al. (47) suggest this as a possible mechanism in their measurements on different stoichiometries of single-crystal YBCO. They found that the pyroelectric response increases with added oxygen content, applied electric field, and prior poling. Another report by Kumar et al. (51) examined the effects of temperature cycling on the properties of metallic YBCO thin films as measured by the photopyroelectric effect. Most relevant to this experiment is the changing of the charge carrier properties with respect to temperature, caused by thermal annealing at 325 K. At this temperature, the oxygen organization in the CuO planes changes as does the density of carriers near the Fermi surface. Furthermore, the changes in these properties do not reverse with respect to temperature for an extended period of time. The result is annealing-in-

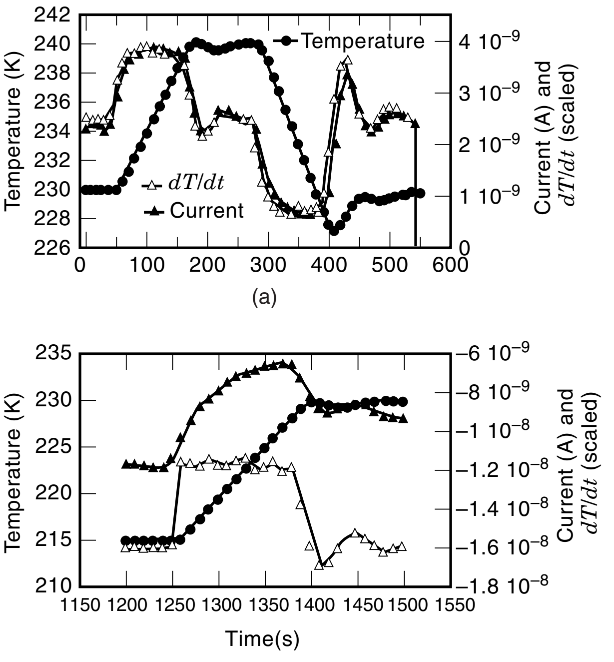

(a)

(b)

Figure 9. (a) Pyroelectric response of YBCO planar capacitor from 230 K to 240 K. $p \approx 400$ nC/(cm$^2 \cdot$ K). (b) Pyroelectric response of the same device after poling at 5000 V/cm at 320 K for 1 h. $p \approx 18$ μC/(cm$^2 \cdot$ K).

duced hysteresis in the thermal and electronic characteristics with respect to temperature.

Figure 9(a) shows the pyroelectric response of a YBaCuO planar capacitor from 230 K to 240 K. $p \approx 400$ nC/(cm$^2 \cdot$ K). Figure 9(b) is the pyroelectric response of the same device after poling at 5000 V/cm at 320 K for 1 h. $p \approx 18$ μC/(cm$^2 \cdot$ K).

Voltage responsivity R_V, detectivity D^*, and noise V_n versus chopper frequency at room temperature is shown in Fig. 10 for a semiconducting YBaCuO layer sandwiched between two Nb electrodes, fabricated on top of a thermally isolated SiO$_2$ bridge. Theoretical fit to Eq. (20) is depicted as the dashed line.

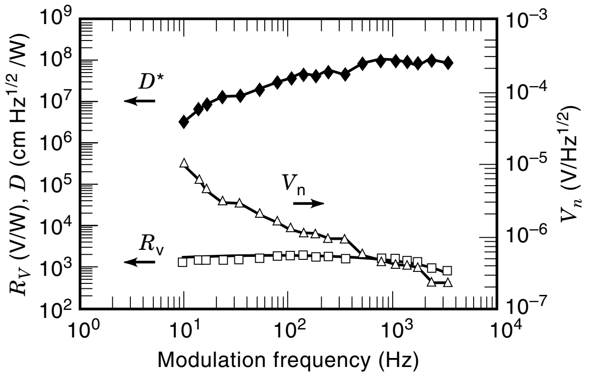

Figure 10. Voltage responsivity R_V, detectivity D^*, and noise V_n for a suspended Nb/YBaCuO/Nb pyroelectric detector versus chopper frequency at room temperature. Theoretical fit to $R_V = \omega pAR\eta/G[(1+\omega^2\tau_e^2)(1+\omega^2\tau_{th}^2)]^{1/2}$ is shown as the dashed line.

SUMMARY

The recent accomplishments in the development of microbolometer and pyroelectric detector arrays for uncooled infrared have demonstrated that high-performance cameras that are more economical for consumer applications are a reality. Although the detectivity of uncooled cameras will always be lower than their cryogenic counterparts, the achievement of NEDTs of 30 mK or less is superior to current HgCdTe technology. The performance of these uncooled cameras is suitable for a large number of consumer applications for night vision in transportation, policing and security, as well as for thermal imaging in medicine. The commercial revenue for uncooled infrared cameras was expected to grow to be in excess of $100 million by the year 2001 (52). With the growth of the market and consumer demand, the cost of the cameras is expected to fall to be within reach of the mass consumer application of automotive night vision. As the market grows, new materials that offer fabrication and performance advantages over the current technologies will be developed.

ACKNOWLEDGMENTS

We would like to express our thanks to William Radford of Hughes Santa Barbara Research Center, Charles Marshall of Lockheed Martin Infrared Systems, and Charles Hanson of Raytheon–TI Systems.

BIBLIOGRAPHY

1. K. C. Liddiard, Thin-film resistance bolometer IR detectors—II, *Infrared Phys.,* **26**: 43–49, 1986.
2. A. Tanaka et al., Infrared focal plane array incorporating silicon IC process compatible bolometer, *IEEE Trans. Electron Devices,* **43**: 1844–1850, 1996.
3. T. A. Enuka et al., Amorphous silicon and germanium films for uncooled microbolometers, *Tech. Phys. Lett.,* **23**: 504–506, 1997.
4. V. Y. Zerov et al., Bolometric properties of silicon thin-film structures fabricated by plasmachemical vapor-phase deposition, *Tech. Phys. Lett.,* **23**: 481–483, 1997.
5. W. Radford et al., 320 × 240 silicon microbolometer uncooled IR-FPAs with on-chip offset correction, *Proc. SPIE,* **2746**: 82–92, 1996.
6. C. Marshall, et al., Uncooled infrared sensor with digital focal plane array, *Proc. SPIE,* **2746**: 23–31, 1996.
7. R. J. Herring and P. E. Howard, Design and performance of the ULTRA 320 × 240 uncooled focal plane array and sensor, *Proc. SPIE,* **2746**: 2–12, 1996.
8. W. Meyer et al., Ambers's uncooled microbolometer LWIR camera, *Proc. SPIE,* **2746**: 13–22, 1996.
9. R. A. Wood, High performance infrared thermal imaging with monolithic silicon focal planes operating at room temperature, *Int. Electron Devices Meet.,* Washington, DC, 1993, pp. 175–177.
10. P. C. Shan et al., Semiconducting YBaCuO thin films for uncooled bolometers, *J. Appl. Phys.,* **78**: 7334, 1995.
11. P. C. Shan et al., The investigation of semiconducting YBaCuO thin films: A new room temperature bolometer, *J. Appl. Phys.,* **80**: 7118–7123, 1996.
12. C. M. Travers et al., Fabrication of semiconducting YBaCuO surface micromachined bolometer arrays, *IEEE/ASME J. Microelectromech. Syst.,* **6**: 271–276, 1997.

13. A. Jahanzeb et al., A semiconductor YBaCuO microbolometer for room temperature IR imaging, *IEEE Trans. Electron Devices,* **44**: 1795–1801, 1997.
14. J. D. Vincent, *Fundamentals of Infrared Detector Operation and Testing,* New York: Wiley, 1990, chap. 1.
15. B. R. Johnson et al., $YBa_2Cu_3O_7$ superconducting microbolometer arrays fabricated by silicon micromachining, *IEEE Trans. Appl. Supercond.,* **3**: 2856, 1993.
16. J. P. Rice et al., High-T_c superconducting antenna-coupled microbolometer on silicon, *Proc SPIE,* **2159**: 98–109, 1994.
17. R. T. Howe, Surface micromachining for microsensors and microactuators, *J. Vac. Sci. Technol.,* **B6**: 1809, 1988.
18. F. N. Hooge, $1/f$ Noise is no surface effect, *Phys. Lett.,* **29A**: 139, 1969.
19. A. van der Ziel, Flicker noise in semiconductors: Not a true bulk effect, *Appl. Phys. Lett.,* **33**: 883, 1978.
20. For a review article see G. Yu and A. J. Heeger, Photoinduced charge carriers in insulating cuprates: Fermi glass insulator, metal-insulator transition and superconductivity, *Int. J. Mod. Phys. B,* **7**: 3751, 1993.
21. Z. Çelik-Butler, W. Yang, and D. P. Butler, Measurements of noise and temperature coefficient of resistance on YBaCuO thin films in magnetic field, *Appl. Phys. Lett.,* **60**: 246, 1992.
22. A. Jahanzeb et al., Studies and implications of the Hall-effect in superconducting and semiconducting $YBa_2Cu_3O_{7-\infty}$ thin films, *J. Appl. Phys.,* **78**: 6658, 1995.
23. Z. Çelik-Butler et al., Charge transport in amorphous and tetragonal semiconducting YBCO films, *Solid State Electron.,* **41**: 895–899, 1997.
24. P. C. Shan et al., Hall-effect in semiconducting epitaxial and amorphous Y–Ba–Cu–O thin films, *J. Appl. Phys.,* **81**, 6866–6873, 1997.
25. B. I. Craig et al., Anisotropic excess noise within *a*-Si:H, *Solid State Electron.,* **39** (6): 807–812, 1996.
26. R. W. Whatmore, Pyroelectric devices and materials, *Rep. Prog. Phys.,* **49**: 1335–1386, 1986.
27. A. Hossain and M. H. Rashid, Pyroelectric detectors and their applications, *IEEE Trans. Ind. Appl.,* **27**: 824–829, 1991.
28. D. E. Marshall, A review of pyroelectric detector technology, *Proc. SPIE,* **132**: 110–118, 1978.
29. C. M. Hanson, Hybrid Pyroelectric–Ferroelectric Bolometer Arrays, in D. Skatrud and P. W. Kruse (eds.) *Semiconductors and Semimetals,* San Diego, CA: Academic Press, Vol. 47, 1997.
30. P. W. Kruse, A comparison of the limits to the performance of thermal and photon detector imaging arrays, *Infrared Phys. Technol.,* **36**: 869–882, 1995.
31. M. C. Foote et al., Transition edge $YBa_2Cu_3O_{7-x}$ microbolometers for infrared staring arrays, *Proc. SPIE,* **2159**: 2, 1994.
32. B. M. Kulwicki et al., Pyroelectric imaging, *IEEE Symp. Appl. Ferroelectr.,* Aug. 1992.
33. J. M. Herbert, *Ferroelectric Transducers and Sensors,* New York: Gordon and Breach, 1982, pp. 266–290.
34. R. L. Byer and C. B. Roundy, Pyroelectric coefficient direct measurement technique and application to a nsec response time detector, *Ferroelectrics,* **3**: 333–338, 1972.
35. J. Mantese et al., Infrared imaging using uncooled focal plane arrays of unreticulated, 10 μ potassium tantalum niobate films, *IEEE Trans. Electron Devices,* **40**: 320–324, 1993.
36. C. Ye, T. Tamagawa, and D. L. Polla, Experimental studies on primary and secondary pyroelectric effects in $Pb(Zr_xTi_{1-x})O_3$, $PbTiO_3$, and ZnO thin films, *J. Appl. Phys.,* **70**: 5538–5543, 1991.
37. L. Pham et al., Surface micromachined pyroelectric infrared imaging array with vertically integrated signal processing circuitry, *IEEE Trans. Ultrason. Ferroelectr. Freq. Control,* **41**: 552–555, 1994.
38. R. Watton and M. A. Todd, Induced pyroelectricity in sputtered lead scandium tantalate films and their merit for IR detector arrays, *Ferroelectrics,* **118**: 279, 1991.
39. C. Bjormander, A. M. Grishin, and K. V. Rao, Pyroelectric $PbSc_{0.5}Ta_{0.5}O_3/YBa_2Cu_3O_{7-x}$ thin film structures, *Appl. Phys. Lett.,* **61**: 58, 1995.
40. C. M. Hanson et al., Uncooled thermal imaging at Texas Instruments, *Proc. SPIE Int. Soc. Opt. Eng.,* 1992, pp. 1–10.
41. R. Takayama et al., Pyroelectric properties and application to infrared sensors of $PbTiO_3$, $PbLaTiO_3$ and $PbZrTiO_3$ ferroelectric thin films, *Ferroelectrics,* **118**: 325–342, 1991.
42. S. T. Liu, J. D. Heaps, and O. N. Tufte, The pyroelectric properties of the lanthanum-doped ferroelectric PLZT ceramics, *Ferroelectrics,* **3**: 281–285, 1972.
43. K. K. Deb, Investigation of pyroelectric characteristics of modified $PbTiO_3$ ceramics for improved IR detector performance, *Ferroelectrics,* **88**: 167–176, 1988.
44. A. Jahanzeb et al., Strong pyroelectric response in semiconducting Y–Ba–Cu–O and its application to uncooled infrared detection, *Appl. Phys. Lett.,* **70**: 3495–3497, 1997.
45. J. E. Gray, Z. Çelik-Butler, and D. P. Butler, Dielectric and pyroelectric response in Nb/YBaCuO/Nb heterostructures, *Ferroelectrics,* 1998.
46. D. Mihailovic and A. J. Heeger, Pyroelectric and piezoelectric effects in single crystals of $YBa_2Cu_3O_{7-\delta}$, *Solid State Commun.,* **75**: 319–323, 1990.
47. D. Mihailovic, I. Poberaj, and A. Mertelj, Characterization of the pyroelectric effect in $YBa_2Cu_3O_{7-\delta}$, *Phys. Rev. B,* **48**: 16,634–16,640, 1993.
48. A. I. Grachev and I. V. Pleshakov, Pyroelectric voltages in YBCO thin films, *Solid State Commun.,* **101**: 507–512, 1997.
49. I. Poberaj and D. Michailovic, Pyroelectric effect measurements in $YBa_2Cu_3O_{6+y}$ and La_2CuO_4 materials, *Ferroelectrics,* **128**: 197–200, 1992.
50. D. Mihailovic and C. M. Foster, Anharmonicity and frequency shift of the apex oxygen O(4) Raman mode in $YBa_2Cu_3O_{7-\delta}$ as a function of doping, *Solid State Commun.,* **74**: 753, 1990.
51. S. Kumar et al., Effect of thermal cycling on normal state thermal properties of $YBa_2Cu_3O_{7-x}$ films, *Physica C,* **215**: 286–290, 1993.
52. E. Cochran, Research Technologies, private communication.

ZEYNEP ÇELIK-BUTLER
DONALD P. BUTLER
Southern Methodist University